Supporting Information

CO$_2$ and CH$_4$ conversion in "real" gas mixtures in a gliding arc plasmatron: How do N$_2$ and O$_2$ affect the performance?

Joachim Slaets, Maryam Aghaei, Sara Ceulemans, Senne Van Alphen and Annemie Bogaerts

Research group PLASMANT, Department of Chemistry, University of Antwerp,

Universiteitsplein 1, BE-2610 Wilrijk-Antwerp, Belgium

E-mail: Joachim.Slaets@uantwerpen.be; Annemie.Bogaerts@uantwerpen.be

Table of Contents

1   Experiments

1.1   Experimental setup and measuring procedure

Figure S.1 shows a schematic overview of the experimental setup. The gas circuit, indicated in blue in the scheme, starts from the individual gas bottles of N_2, CO_2, CH_4 and O_2. The flow of every gas is individually regulated by a mass flow controller (MFC) (Bronkhorst), connected to and operated by a computer. The gases mix in the main inlet tube connected to the reactor. The gas mixture enters the reactor through six tangential inlets, each with a diameter of 1.6 mm.
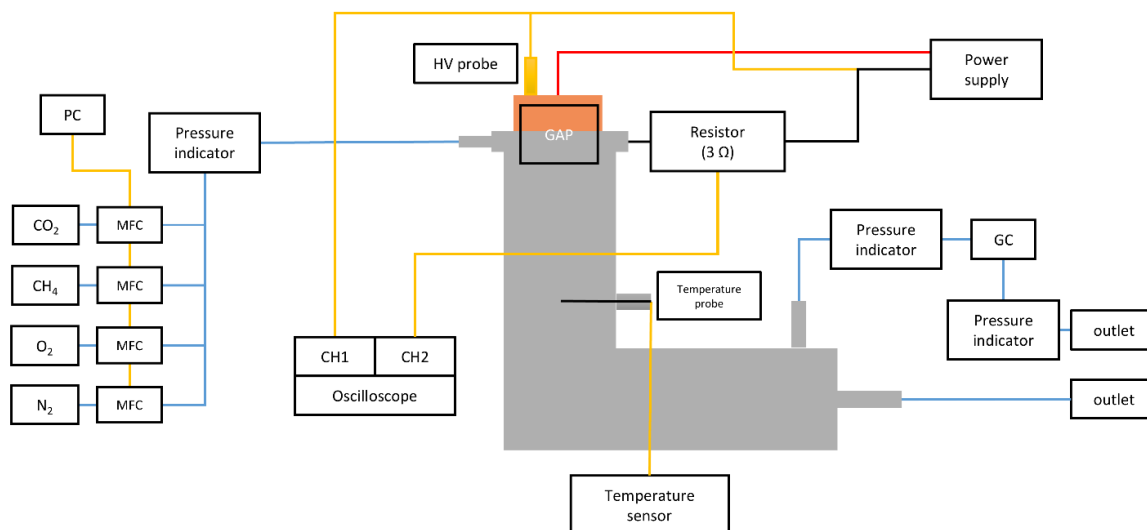
Figure S.1: *Schematic overview of the experimental setup.*

The gliding arc plasmatron (GAP) reactor is made up of two major parts, i.e., the cathode and anode, separated by a Teflon ring for insulation. Figure S.2 provides a schematic cross section of the GAP reactor, with all dimensions indicated. The cathode has a length and inner diameter of 10.99 mm and 17.53 mm, respectively. The anode has a length of 16.51 mm and inner diameter of 7.07 mm.
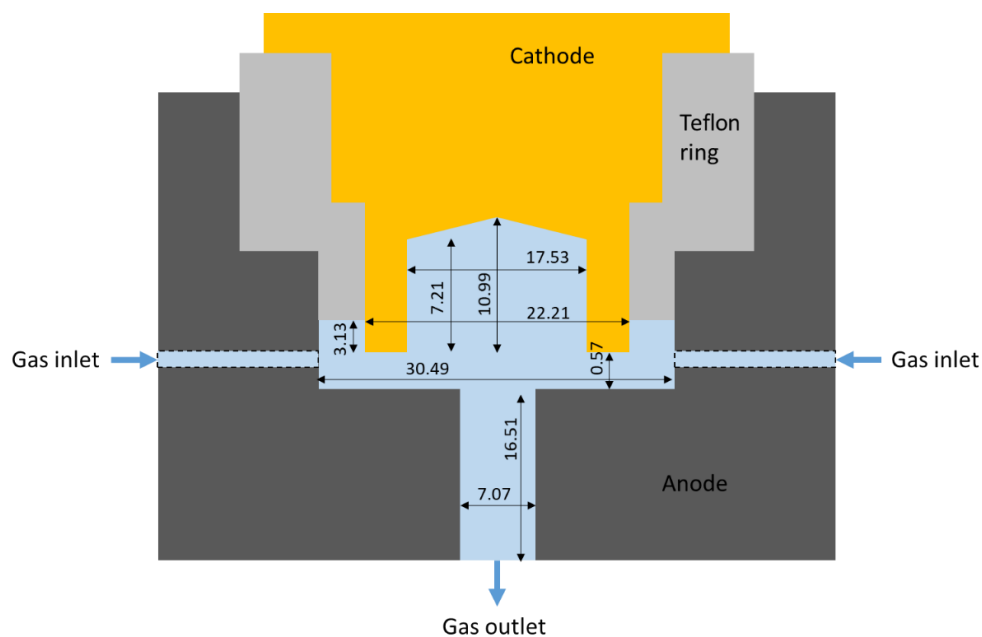
Figure S.2: *Schematic cross section of the gliding arc plasmatron (GAP) reactor, with dimensions in mm (not scaled).*

The plasma arc is created between cathode and anode, as illustrated in Figure 1 of the main paper. The cathode is connected to the high voltage wire (indicated in red in Figure S.1) of the power supply (Advanced Plasma Solutions, PA, USA) and the anode is connected to the ground. The gas leaves through the anode after passing through the reactor body (cathode) in a forward and reverse vortex flow (cf. Figure 1 of the main paper). The exhaust of the reactor is connected to the grey L-shaped tube in Figure S.1, where part of the gas will leave the setup through the outlet and is removed by the fume hood in which the setup is placed. The rest of the gas enters the gas chromatograph (GC) (Thermo Scientific trace 1310 GC) and a thermal conductivity detector (TCD) for the gas analysis. A detailed description of the GC measurements is given below.

The plasma power was obtained by measuring the voltage and current passing through the arc, using an oscilloscope (Tektronix TDS2012C) added to the electrical circuit (as indicated in S.1). The voltage was measured using a high voltage probe (Testec) connected to the cathode, the ground wire and channel 1 of the oscilloscope. The current was measured using a 3 Ohm resistor in the ground wire, which is connected to channel 2 of the oscilloscope. This yields a potential, which is converted into current, using $I = V/R$ with the resistance R = 3 Ohm. The plasma power was obtained by integrating the product of potential and current over a certain period of time.

A temperature probe was inserted into the L-shaped tube after the reactor (see also Figure S.1) to monitor the temperature of the outflowing gas at a distance of 26 cm of the exhaust of the reactor. This can give an indication of the gas temperature changes in the reactor upon O_2 addition, although it must be realized that the temperature inside the GAP will be much higher (i.e., order of 2000-3000 K).[1] Finally, several pressure sensors were placed along the gas circuit to monitor the correct working of the setup during the experiments.

The exhaust gases were analysed using a gas chromatograph (Thermo Scientific trace 1310 GC) for the gas separation and a thermal conductivity detector (TCD) for the gas detection. During the measurement, the gases enter the GC and are stored in sample loops, each with a volume of 100 µL, placed in the valve oven. In total, there are 10 sample loops, but the first and the last ones are reserved as buffer between two measurements to prevent overflow from one to another. The remaining eight loops are filled and can be measured. In fact, in order to increase the accuracy of the measurements, we performed the entire experiment in triplicate, and we measured only the first four sample valves, rather than measuring more valves from one single experiment.

After the filling process, the samples were one by one injected with helium as carrier gas in a set of three columns in series for separation. These columns were placed in a second oven. The first column is a porous layered open tubular column (Rt-Q-BOND) with a divinylbenzene stationary phase. This column is responsible for the separation of CO_2 and CH_4 from O_2, N_2 and CO. The second column is the same as the first one to increase the separation capabilities. The third column uses a zeolite packing stationary phase (Molsieve 5A) to separate inert gases (e.g., He, Ar) and light gases (e.g., O_2, N_2, CH_4, CO, H_2).

The last step in the gas analysis is the detection of the different components, by means of a TCD. Every gas has its own thermal conductivity, which makes this detector very versatile in the detection of different compounds.[2] The TCD consists of two fixed resistors and two thermal resistors that are arranged in a Wheatstone bridge circuit.

1.2   *Safety analysis of the gas mixtures under study*

The different fractions of CH_4, CO_2, O_2 and N_2 in the mixture, used to test the performance of the GAP reactor, are listed in Table S.1. As the addition of O_2 to a mixture containing CH_4 could form an explosive mixture, every mixture was checked carefully to be out of the explosion regime. The O_2 concentration ($O_2/(O_2+N_2+CO_2)$) was lower than 21 % for all mixtures, and therefore the flammability limits in air could be used.[3] The CH_4 concentration needs to be above or below a certain value, depending on the O_2 concentration. There is no explosion risk for O_2 concentrations below 13 %. However, some

of the mixtures in our study contain O_2 concentrations above 13 %, but they are also safe to use as the CH_4 concentrations are above the explosion limit.[3]

Alternatively, a ternary flammability diagram for the mixture of N_2, CH_4 and O_2 can also be consulted to determine whether it is safe to use the gas mixtures in our study. We could not find a diagram for the combination of CO_2, N_2, CH_4 and O_2, so we used a diagram with only N_2 as passive agent, although in our case CO_2 and N_2 are both taken as passive agents.[4] All the used gas mixtures (cf. Table S.1) are indeed safe to use according to this diagram. It should be noted that the flammability region is smaller for a mixture with only CO_2 as passive agent, which gives us an extra safety margin for our experiments, as we used a combination of N_2 and CO_2.

The gas flow rate was set for every gas individually to achieve a total fixed gas flow rate of 10 L min^{-1}. Before the plasma was turned on, the reactor was flushed for 5 minutes with the gas mixture, to replace the air in the reactor and tubes. The current on the power supply was increased until the plasma was ignited, after which the current was kept manually at 300 mA. The plasma was left to stabilize for 10 minutes before filling the sample loops of the GC. During the filling process, the oscilloscope data was saved typically around 5 to 7 times to obtain the average plasma power for one measurement. At the same time, the temperature from the thermocouple was recorded. The plasma was turned off and the reactor was left to cool down for the next experiment, while the GC was measuring the sample loops. For every condition, the plasma was measured in triplicate for statistical relevance. These results were compared to a blank measurement for which no power was applied and no plasma was created. By comparing the data with plasma with those from the blank measurement, we can calculate the gas conversion, as explained below.

Table S.1: *Overview of the tested gas mixtures.*

CH_4 (%)	CO_2 (%)	O_2 (%)	N_2 (%)	CH_4/CO_2	O_2/CH_4
10	10	11	69	1	1.1
10	10	9	71	1	0.9
10	10	7	73	1	0.7
10	10	5	75	1	0.5
10	10	3	77	1	0.3
10	10	0	80	1	0.0
15	10	16.5	58.5	1.5	1.1
15	10	13.5	61.5	1.5	0.9
15	10	10.5	64.5	1.5	0.7
15	10	7.5	67.5	1.5	0.5
15	10	4.5	70.5	1.5	0.3
15	10	0	75	1.5	0.0

1.3 Analysis of the results

The absolute conversion (χ_{abs}) was calculated for CO_2 and CH_4 using Equation (1), in which i is the molecule (CO_2 or CH_4 in this case), $A_{i_{blank}}$ is the peak area of the blank measurement, $A_{i_{plasma}}$ is the peak area of the plasma measurement and α is a correction factor for gas expansion.[5] All of the peak areas are averaged values from the four sample loops that were analysed by the GC.

$$\chi_{abs_i}(\%) = \frac{A_{i_{blank}} - \alpha \cdot A_{i_{plasma}}}{A_{i_{blank}}} \cdot 100 \% \tag{1}$$

A correction factor α was used in the conversion equation to correct for gas expansion.[6] Indeed, DRM leads to an expansion of gas due to the increasing number of molecules after the reaction (see equation in the Introduction of the main paper). As a result, the volumetric flow rate also increases. The sample loops in the GC, however, have a constant volume, and therefore gas expansion will result in a pressure rise. However, the GC operates at atmospheric pressure, meaning that part of the gas is lost before injecting in the GC. This results in a lower number of molecules (e.g., of CO_2 or CH_4) being detected compared to the number of molecules in the outlet of the reactor, which leads to an overestimation of the conversion. Most papers on plasma-based gas conversion do not account for this expansion factor and therefore report an overestimated conversion.[6]

The expansion factor can be determined by adding an internal standard, such as N_2, He or Ar, to the outflow gas stream after the gas has passed through the reactor. He cannot be used as this is the carrier gas in the GC. Neither can Ar, because the peak overlaps with the one of O_2. In principle, N_2 is also not possible, because it is introduced in the gas mixture that passes through the GAP reactor. However, in practice, the conversion of N_2 in the GAP is very limited and could be neglected. The factor α is thus defined as the ratio of the N_2 peak area from the blank to the plasma measurement [Eq. (2)].[5]

$$\alpha = \frac{A_{N_2,blank}}{A_{N_2,plasma}} \qquad (2)$$

The absolute conversion defines the amount of converted gas by comparing the blank and the plasma measurements. However, due to dilution with other gases in the mixture, we also define the effective conversion, which accounts for the fraction of component i in the initial gas mixture [Eq. (3)].[5]

$$\chi_{eff_i}(\%) = \chi_{abs_i}(\%) \cdot fraction_i \qquad (3)$$

The total conversion (χ_{total}) [Eq. (4)] is calculated as the sum of the effective conversions of CO_2 and CH_4.[5]

$$\chi_{total}(\%) = \chi_{eff_{CO_2}}(\%) + \chi_{eff_{CH_4}}(\%) \qquad (4)$$

The yields (Y in %) of the different products are calculated from the effective conversions of CH_4 and CO_2 and the product selectivities. The selectivity (S in %) is calculated based on C for all the products [Eq. (5)], except for H_2, H_2O and H_2O_2, for which we calculated the H-based selectivity [Eq. (6)].[7] In these equations general notations are used for the products ($C_xH_yO_z$ and H_yO_z) in which x, y and z are the number of C, H and O atoms in the products, c is the concentration (in %) and α is the correction factor for gas expansion (discussed above, see Eq. (2)). The yields are calculated using Equations (7, 8).[7]

$$S_{C,C_xH_yO_z}(\%) = \frac{x \cdot c_{C_xH_yO_z (out)} \cdot \alpha}{\left(c_{CH_4 (in)} - c_{CH_4 (out)} \cdot \alpha\right) + \left(c_{CO_2 (in)} - c_{CO_2 (out)} \cdot \alpha\right)} \cdot 100 \% \qquad (5)$$

$$S_{H,H_yO_z}(\%) = \frac{y \cdot c_{H_yO_z (out)} \cdot \alpha}{4 \cdot \left(c_{CH_4 (in)} - c_{CH_4 (out)} \cdot \alpha\right)} \cdot 100 \% \qquad (6)$$

$$Y_{C_xH_yO_z}(\%) = \left(X_{eff,CH_4} + X_{eff,CO_2}\right) \cdot \frac{1}{x} \cdot S_{C,C_xH_yO_z} \qquad (7)$$

$$Y_{H_yO_z}(\%) = \left(4 \cdot X_{eff,CH_4}\right) \cdot \frac{1}{y} \cdot S_{H,H_yO_z} \qquad (8)$$

The specific energy input (SEI) is calculated using Equations (9, 10), in which P_{plasma} is the plasma power calculated from the oscilloscope data (described above), V_{mol} is the molar volume (24.5 L mol^{-1} at 293 K) and Q is the total gas flow rate (10 L min^{-1}).[5]

$$SEI (kJ L^{-1}) = \frac{P_{plasma}(kW) \cdot 60(s\ min^{-1})}{Q(L\ min^{-1})} \qquad (9)$$

$$SEI (eV\ molecule^{-1}) = SEI(kJ\ L^{-1}) \cdot \frac{6.24 \cdot 10^{21}(eV\ kJ^{-1}) \cdot V_{mol}(L\ mol^{-1})}{6.022 \cdot 10^{23}(molecule\ mol^{-1})} \qquad (10)$$

The energy cost of the conversion (EC_i) can be calculated either for the individual gas conversions (where i can be CO_2 or CH_4) or for the total conversion, using Equations (11, 12).[5]

$$EC_{total}(kJ\ L^{-1}) = \frac{SEI\ (kJ\ L^{-1})}{\chi_{total}} \tag{11}$$

$$EC_{total}(eV\ molecule^{-1}) = EC_{total}(kJ\ L^{-1}) \cdot \frac{6.24 \cdot 10^{21}(eV\ kJ^{-1}) \cdot V_{mol}(L\ mol^{-1})}{6.022 \cdot 10^{23}(molecule\ mol^{-1})} \tag{12}$$

The results presented (both in the main paper and in this SI) are provided with their calculated error bars, to show the uncertainty on the results. The plasma power is measured multiple times (typically six times) during one experiment, to obtain the average power for one measurement, along with the corresponding error. The same is done for the peak areas obtained from the GC. In the formulas where flow rate is required, the error on the MFC's is taken into account. For every experiment, the conversion, SEI and energy cost were determined. The experiments were performed in triplicate, which allows to take the weighted average as the final result for one condition.

2 Computational part

2.1 Description of the 0D plasma chemical kinetics model

The plasma chemistry was described with the Zero-Dimensional Plasma Kinetics solver (ZDPlasKin).[8] In this model the mass conservation equations for all individual species are solved. Every species in the plasma has a certain number density (expressed in m^{-3}) that changes as a result of the occurring plasma reactions. Part of the species will be consumed by reactions (loss term) and part will be formed from other reactions (production term). The evolution of the species densities over time is calculated by solving Equation (13) for every species, in which n_s is the density of species s (in m^{-3}), j is the number of reactions included in the model in which this species is either formed or lost, $a_{s,i}^R$ and $a_{s,i}^L$ are the stoichiometric coefficients at the right and left side of the reaction equation (corresponding to production and loss term), respectively, and R_i is the rate of the reaction (in $m^{-3}\ s^{-1}$). The latter is calculated from the reaction rate constant (k_i) multiplied with the densities of the reacting species j, using Equation (14).

$$\frac{\partial n_s}{\partial t} = \sum_{i=1}^{j}\left[(a_{s,i}^R - a_{s,i}^L)R_i\right] \tag{13}$$

$$R_i = k_i \prod_j n_j^{a_{s,i}} \tag{14}$$

The reaction rate constant (k_i) is given in a different form depending on the type of reaction. For reactions between heavy particles (neutrals, ions, radicals) the rate constant is either a constant value or a function of the gas temperature. These constants are taken from the literature.[5,9,10] The rate constants for electron impact reactions, on the other hand, are calculated using the Boltzmann solver, BOLSIG+, built into ZDPlasKin.[11] This Boltzmann subroutine in the code calculates the Boltzmann equation for the electrons in a fixed reduced electric field (i.e., ratio of electric field over gas number density) using a two-term approximation, yielding the electron energy distribution function (EEDF). From the EEDF the mean electron energy is obtained and the various electron impact rate coefficients are calculated using Equation (15), in which ϵ is the electron energy (in J), ϵ_{th} is the minimal energy needed for the reaction to occur, $\sigma(\epsilon)$ is the collision cross section (in m^2), $f_e(\epsilon)$ is the EEDF (in J^{-1}) and $v(\epsilon)$ is the velocity of the electron with energy ϵ (in $m\ s^{-1}$). The collision cross sections were taken from literature.[5,9,10] The electron velocity is calculated with Equation (16), in which m_e is the electron mass ($9.10938 \cdot 10^{-31}$ kg).

$$k = \int_{\epsilon_{th}}^{+\infty} \sigma(\epsilon)f_e(\epsilon)\ v(\epsilon)d\epsilon \tag{15}$$

$$v(\epsilon) = \sqrt{\frac{2\epsilon}{m_e}} \tag{16}$$

The plasma power obtained from the experiments was used as input for the 0D model to calculate the electric field (E) (in V m^{-1}), with Equation (17) in which P is the plasma power (in W), V_{plasma} is the total plasma (arc) volume, defined in this work as the volume of a cylinder with certain length and radius: $V_{plasma} = r_{arc}^2 \cdot \pi \cdot l_{arc}$ (in m^3), and σ is the plasma conductivity (in A V^{-1} m^{-1}). The plasma conductivity is calculated using Equation (18), with μ_{red} the reduced electron mobility (in m^{-1} V^{-1} s^{-1}), obtained from the BOLSIG+ solver, n_{tot} the total density of all plasma species (in m^{-3}), n_e the electron density (in m^{-3}) and e the elementary charge ($1.60217662 \cdot 10^{-19}$ C).

$$E = \sqrt{\frac{P}{V_{plasma} \cdot \sigma}} \tag{17}$$

$$\sigma = \frac{\mu_{red}}{n_{tot}} \cdot n_e \cdot e \tag{18}$$

2.2 Plasma chemistry included in the model

The plasma chemistry in the 0D model is defined by a set of plasma species and set of reactions between them. The largest benefit of the 0D model is the ability to handle a large number of species and reactions within reasonable calculation time. Allowing for a detailed chemistry set makes this a very interesting model.

The species taken into account in the model, which can be formed from the gas mixture of N_2, CO_2, CH_4 and O_2, are listed in Table S.2. This includes various ions, radicals, excited species and molecules, as well as the electrons. These species interact with each other in 16210 reaction, i.e., various electron impact reactions, electron-ion recombination reactions, ion-ion, ion-neutral, and neutral-neutral reactions, as well as vibrational-translational and vibrational-vibrational relaxation reactions. This type of model has been used to simulate a wide range of different plasmas and applications, among which CO_2 conversion and DRM.[5,12–14]

The reactions (and corresponding rate coefficients) between CH_4 and CO_2 derived species (hence including also those between CH_4 and O_2 derived species) were taken from Cleiren et al.[5], the reactions between CO_2 and N_2 derived species (including also those between O_2 and N_2 derived species) were adopted from Ramakers et al.[9], and those between CH_4 and N_2 from Snoeckx et al.[10]

Note that the number of species and chemical reactions in this model is much larger than what is actually needed for the purpose of this study, as we are in first instance interested in the conversion of CH_4 and CO_2, and the effect of N_2 and O_2 on these conversions, but not in the formation of all possible reaction products. However, this chemistry set was developed to be as complete as possible, because it is not *a priori* known which species and chemical reactions are important in the conversion process. For instance, the model contains a large number of (electronically and vibrationally) excited levels, which can be important for the energy-efficient CO_2 conversion.

Table S.2: Species included in the 0D model, sorted by type.

Neutral species	Ions	Radicals	Excited species
	electrons		
C_3H_8, C_3H_6		C_3H_7, C_3H_5	
C_2H_6, C_2H_4, C_2H_2	$C_2H_6^+$, $C_2H_5^+$, $C_2H_4^+$, $C_2H_3^+$,	C_2H_5, C_2H_3, C_2H	
	$C_2H_2^+$, C_2H^+		

|			
CH_4	CH_5^+, CH_4^+, CH_3^+, CH_2^+, CH^+	CH_3, CH_2, CH	
H_2	H_2^+		$H_2(V_1-V_{14})$, $H_2(EF1)$, $H_2(B1)$, $H_2(C1)$, $H_2(a3)$, $H_2(c3)$, $H_2(H1)$, $H_2(B'1)$, $H_2(D1)$, $H_2(G1)$, $H_2(I1)$, $H_2(h3)$, $H_2(e3)$, $H_2(d3)$, $H_2(g3)$, $H_2(i3)$
	H^+, H^-, H_3^+	H	H(2), H(3)
N_2	N_2^+		$N_2(V_1-V_{24})$, $N_2(A^3\Sigma_u^+)$, $N_2(B^3\Pi_g)$, $N_2(a^1\Sigma_u^-)$, $N_2(C^3\Pi_u)$
	N^+, N_3^+, N_4^+	N	N(2D), N(2P)
N_2O, N_2O_3, N_2O_4, N_2O_5	NO^+, N_2O^+, NO_2^+, NO^-, N_2O^-, NO_2^-, NO_3^-	NO, NO_2, NO_3	
C_2N_2		CN, NCN, C_2N ONCN, NCO	
CO_2	CO_2^+		$CO_2(V_a-V_d)$, $CO_2(V_1-V_{21})$, $CO_2(E_1)$
CO	CO^+, CO_3^-, CO_4^-, CO_4^+		$CO(V_1-V_{10})$, $CO(E_1-E_4)$
O_2	O^-, O_2^-	O	$O_2(V_1-V_4)$, $O_2(E_1-E_2)$
CH_2O, CH_3OH		CHO, CH_2OH	
CH_3OOH		CH_3O, CH_3O_2	
C_2H_5OH, C_2H_5OOH		C_2HO, CH_3CO	
CH_3CHO, CH_2CO		CH_2CHO, C_2H_5O, $C_2H_5O_2$	
C_3H_7OH			
H_2O, H_2O_2	H_2O^+, H_3O^+, OH^-, OH^+	HO_2, OH	
NH_3, N_3H, N_2H_2 (= HNNH, diazene), N_2H_2 (= H_2NN, isodiazene), N_2H_4		NH, NH_2, N_2H_3	
HNO, HNCO, HNO_2, HNO_3, NH_2OH, NH_2NO		NH_2O, NHOH	
CH_3NH_2, CH_3NHNH_2		CH_3NH	
HCN, CH_3CN, NCCN		H_2CN, H_2NC, CH_2CN, CH_3NCH_3, HCCN	

2.3 Input parameters in the model

The model was set up to simulate the plasma arc inside the GAP reactor. This was done by approaching the arc as a cylinder with a length of 1.15 cm, which is the distance between cathode end and anode

edge of the GAP reactor (see Figure S.2 above), i.e., where the arc is assumed to be attached,[1,15] and a diameter of 0.2 cm, which was obtained from 3D plasma fluid dynamics simulations.[1] In practice, the plasma arc will not be completely homogeneous in the axial and radial direction. The radial non-uniformity is neglected in the 0D model, which is a reasonable assumption, based on the 3D plasma fluid dynamics simulations.[1] In the axial direction, the gas temperature is not uniform. This can, however, be incorporated in the model by converting the time dependence of the model into a position dependence using the axial gas velocity through the arc. To obtain the latter, a velocity profile along the arc was calculated using a 3D fluid dynamics simulation for the GAP reactor, at a gas flow rate of 10 L min^{-1}, from which the average axial velocity of this profile was obtained as 1.98 m s^{-1}.

One of the drawbacks of a 0D model is that it is not self-consistent, meaning that input parameters need to be provided to the model, such as gas temperature, power density and initial gas densities. The initial densities of N_2, CO_2, CH_4 and O_2 were set to the experimental conditions (i.e., gas mixing ratios as listed in Table S.1 above, at 1 atm and the inlet temperature of 293 K; see below), while the other species densities were set to zero. The gas temperature and power density are required as a function of the position in the arc, because the time dependence is converted into a position dependence. The power density can be set to a constant value throughout the arc, defined as the experimental plasma power divided by the arc volume. The gas temperature in the arc cannot be set to a constant value, because it will vary as a function of position (see above), and also be different for different conditions. Therefore, we used the results of 3D fluid dynamics simulations to determine a temperature profile in the arc. Note that the arc was simply represented by a cylindrical heat source with a power input of 400 W (i.e., a typical plasma power of our experiments; see below). A gas flow rate of 10 L min^{-1} was used, the same as in the experiments. A temperature profile for the 0D model was calculated using a weighted average of the high temperature in the core of the arc and the lower temperature at the edges of the arc. This profile, given in Figure S.4, demonstrates that the arc is hotter near the cathode end, and slightly cools down towards the anode edge. This is due to the effect of the hot cathode spot,[1,16] while the gas flowing in the outer vortex just entered the reactor at room temperature, and thus cools the hot gas in the inner vortex (and in the arc).
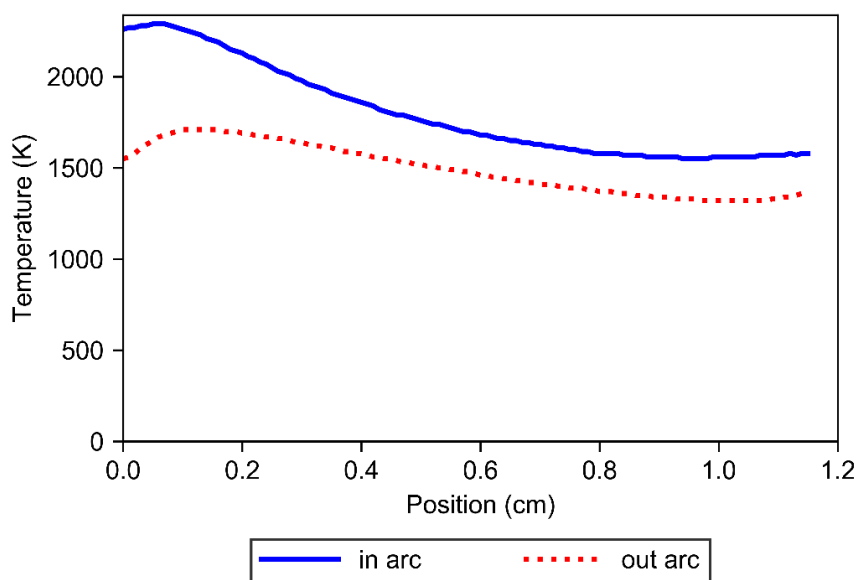
Figure S.3: *Weighted average temperature profiles obtained from the 3D fluid dynamics simulations at a power of 400 W and gas flow rate of 10 L min^{-1}, for both inside the arc (with radius of 0.2 cm) and the area just around the arc (with radius of 0.3535 cm). The cathode end is at 0 cm, while the anode edge is at 1.15 cm.*

This temperature profile is, however, only an approximation that does not take any reactions in the plasma into account. Indeed, such simulations have been carried out before for argon gas in a 3D model, and for CO_2 in a 2D model, but developing such a model for the gas mixture under study would lead to prohibitively long calculation times. Thus, this temperature profile is subject to uncertainty, but due to

lack of more accurate data, we used it as an input for the 0D model, but we applied a certain correction factor to obtain better agreement with the experimentally obtained conversions. However, it must be mentioned that this is the only adaptable parameter, and it still yields a realistic temperature profile. During the experiments, a significant change in gas temperature was observed in the exhaust, depending on the O_2 fraction in the mixture (see Figure 7 in the main paper). Therefore, a correction factor was determined for the lowest and highest O_2 fraction (i.e., multiplying with 1.22 for 0 % O_2, and with 1.38 for 16.5 % O_2), and the remaining correction factors were in between these two. We did not focus on the exact agreement between model and experiments, but as the model shows similar trends as the experiments for conversion, yields and energy cost, for the different gas mixing ratios, we can assume that the chemistry set is sufficiently realistic to be used to explain the plasma chemistry.

2.4   Calculation of conversion, yields and energy cost in the model

The conversion and yields obtained with the model were calculated in a somewhat different way than in the experiments. Two sets of simulations were performed. On the one hand, the model only simulates the arc region, and takes into account that not all of the gas passes through the plasma arc. This is done with Equation (19) in which i is the species for which the conversion is calculated, $n_{i\,(in)}$ and $n_{i\,(out)}$ are the densities of species i at the beginning and the end of the arc, respectively (in m^{-3}), j stands for all the species in the model, $n_{j\,(in)}$ and $n_{j\,(out)}$ are their densities at the beginning and the end of the arc, respectively (in m^{-3}), m_j is the mass of species j (in kg), v_0 is the velocity in the arc (in m s^{-1}), A is the cross sectional area of the simulated region (in m^2) and Q is the gas flow rate (in m^3 s^{-1}).

$$\chi_{abs_i}(\%) = \frac{1 - n_{i\,(out)} \cdot \frac{\sum_j n_{j\,(in)} \cdot m_j}{\sum_j n_{j\,(out)} \cdot m_j}}{n_{i\,(in)}} \cdot 100\ \% \cdot \frac{v_0 \cdot A}{Q} \tag{19}$$

Earlier calculations revealed that only a small fraction of the gas (13.85 %, the last part of the equation) actually passes through the arc,[13] meaning that only a limited overall conversion can be reached, even if the conversion in the arc would be 100 %. However, because the arc heats up the gas around it, an additional simulation of the region around the arc was conducted to study the effect of thermal conversion. The same 3D fluid dynamics simulation provided a temperature profile for the area around the arc, with a radius of 0.3535 cm (i.e., the radius of the exhaust) (see also Figure S.3 above), which is used as input for modelling the thermal conversion, after multiplying with the same factor as for the temperature profile in the arc. The conversion of the model is the sum of both the conversion in the arc and in the thermal area around the arc, scaled to the fraction of gas passing through each region.

The yields (Y in %) obtained from the simulations are calculated with the same formulas as for the experiments, but the selectivities are obtained by slightly different formulas given in Equations (20, 21).

$$S_{C,C_xH_yO_z} = \frac{x \cdot n_{C_xH_yO_z\,(out)} \cdot \frac{\sum_j n_{j\,(in)} \cdot m_j}{\sum_j n_{j\,(out)} \cdot m_j}}{\left(n_{CH_4\,(in)} - n_{CH_4\,(out)} \cdot \frac{\sum_j n_{j\,(in)} \cdot m_j}{\sum_j n_{j\,(out)} \cdot m_j}\right) + \left(n_{CO_2\,(in)} - n_{CO_2\,(out)} \cdot \frac{\sum_j n_{j\,(in)} \cdot m_j}{\sum_j n_{j\,(out)} \cdot m_j}\right)} \cdot 100\ \% \cdot \frac{v_0 \cdot A}{Q} \tag{20}$$

$$S_{H,H_yO_z} = \frac{y \cdot n_{H_yO_z\,(out)} \cdot \frac{\sum_j n_{j\,(in)} \cdot m_j}{\sum_j n_{j\,(out)} \cdot m_j}}{4 \cdot \left(n_{CH_4\,(in)} - n_{CH_4\,(out)} \cdot \frac{\sum_j n_{j\,(in)} \cdot m_j}{\sum_j n_{j\,(out)} \cdot m_j}\right)} \cdot 100\ \% \cdot \frac{v_0 \cdot A}{Q} \tag{21}$$

The syngas ratio is calculated as the ratio of the densities of H_2 and CO_2 at the exhaust. The same approach as for the conversion is also taken for yield and syngas ratio, this is calculated for the simulation in the arc and the thermal region around the arc separately, multiplied with the fraction of gas passing through the respective regions and added together.

The energy cost was calculated with the same formula as in the experiments (see section 1.2 above). The SEI was the same for both the model and the experiments, as the experimental plasma power and gas flow rate were used as input parameters for the model.

3   Results and Discussion

3.1 Total conversion

The total conversion is plotted in Figure S.4. It is calculated as the sum of the individual conversions of CO_2 and CH_4 (see Figure 2 in the main paper), each multiplied with their fraction in the mixture. It increases with rising O_2 fraction and reaches values between 10 and 20 %. These lower values are due to the smaller fractions of CO_2 and CH_4 in the mixture. For an O_2/CH_4 ratio of 1.1, a small drop is observed as a result of the lower CO_2 conversion (cf. Figure 2 in the main paper). A higher CH_4 fraction shows a faster rise in total conversion, due to its higher contribution to the total conversion.
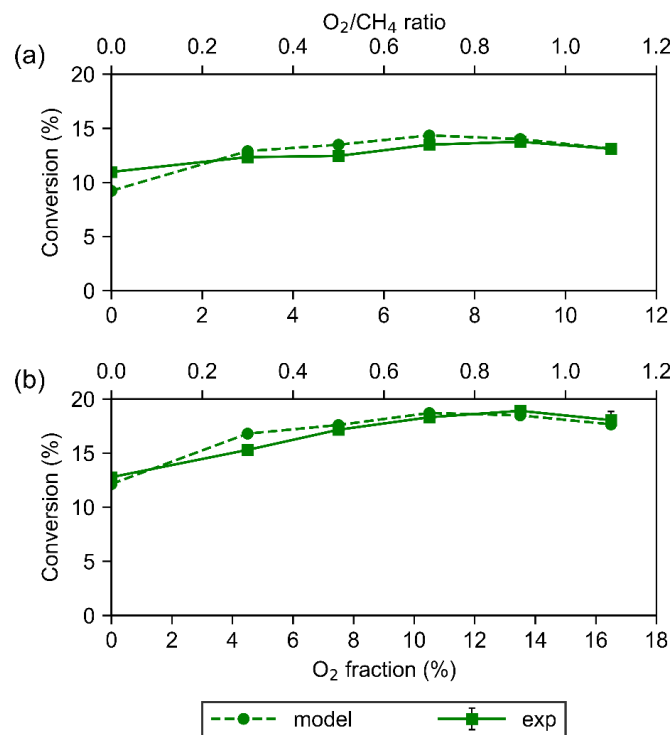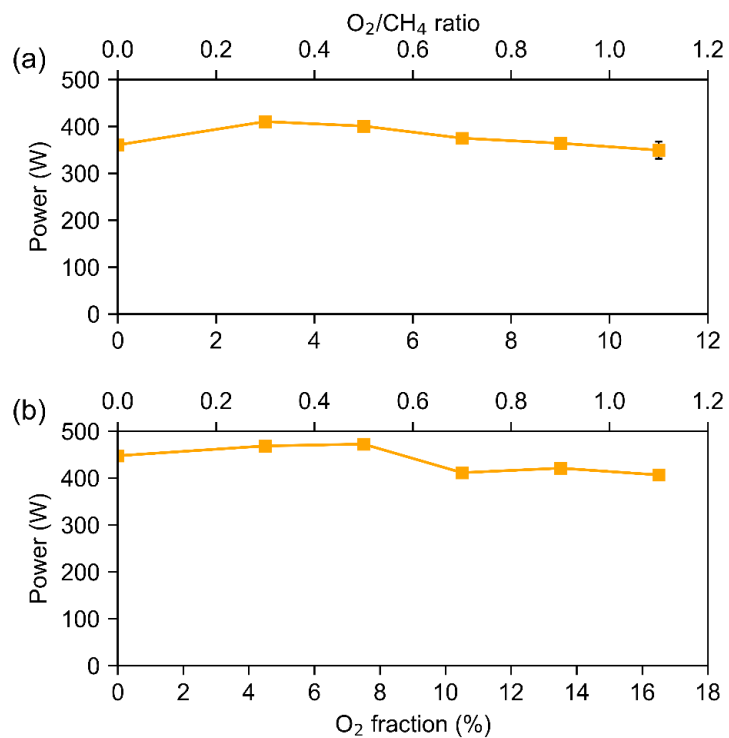

Figure S.4: *Experimental and modelling result for the total conversion as a function of the O_2 fraction and O_2/CH_4 ratio, for a CH_4 fraction of 10 % (a) and 15 % (b). The experiments were performed in triplicate, but the error bars on the experimental results are too small to be visible.*

3.2 Plasma power and SEI

The power was obtained from the potential and current delivered by the power supply. The current through the plasma was manually kept at 300 mA, while the potential was adjusted by the power supply to keep this current. It is clear from Figure S.5 that the power is only slightly different for different gas compositions. Without O_2 present in the mixture, changing the CH_4 fraction does not affect the power. However, when O_2 is present, a higher CH_4 fraction leads to a somewhat higher plasma power. At the same time, increasing the O_2 fraction leads to a slight drop in the power. However, the variations are quite small, and because of the complexity of the different gas mixtures, it is difficult to determine the effect of the individual gases on the plasma power. The fact that the current had to be manually adjusted during the experiments can also give rise to these small variations in plasma power.

The SEI is directly proportional to the plasma power, as the total gas flow rate is constant in these experiments (10 L min^{-1}). It is plotted in Figure S.6 and varies between 0.5 and 0.7 eV molecule^{-1} (or between 2 and 2.8 kJ L^{-1}).

Figure S.5: *Measured plasma power as a function of the O_2 fraction and O_2/CH_4 ratio, for a CH_4 fraction of 10 % (a) and 15 % (b). The error bars are too small to be visible.*
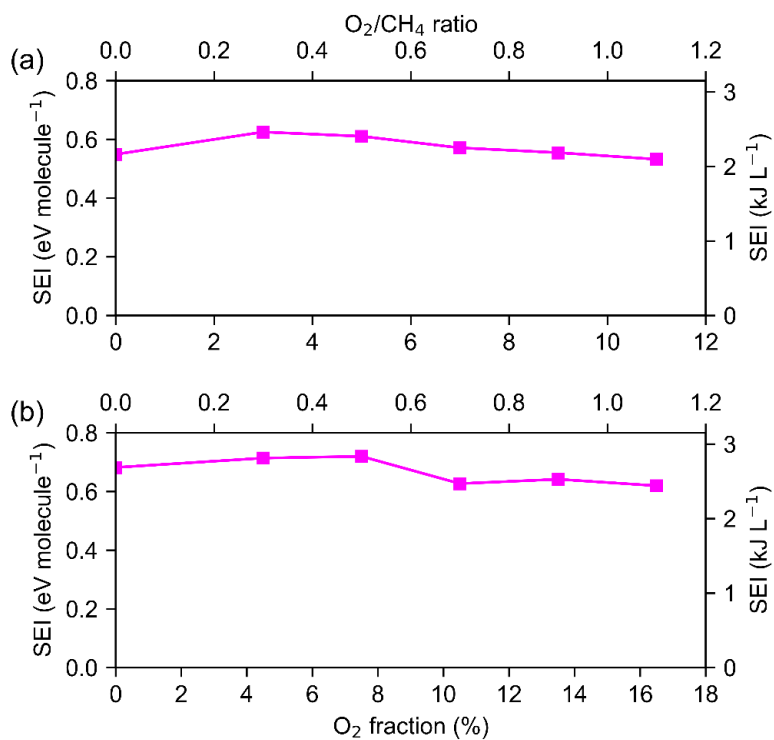
Figure S.6: *Experimentally obtained SEI as a function of the O_2 fraction and O_2/CH_4 ratio, for a CH_4 fraction of 10 % (a) and 15 % (b). The error bars are too small to be visible.*

3.3 Benchmarking our obtained conversion and energy cost with other plasma results from literature

To benchmark our results of energy cost and total conversion, we added them with red dots to Figure S.7, which shows an overview of energy cost vs total conversion for DRM, for a wide range of different plasma types, adopted from[3]. Note that the y-axis of energy cost is reversed, so above the efficiency target and thermal conversion line means lower values of energy cost. See discussion in the main paper.
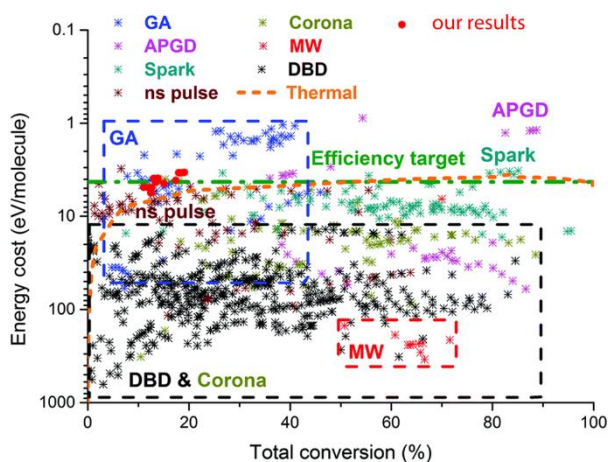

Figure S.7: Comparison of energy cost as a function of total conversion for a range of DRM results from literature.[3] Our results are added to the graph as red dots. Reproduced from Ref. 11 with permission from the Royal Society of Chemistry.

### 3.4 Effect of the gas expansion factor on the conversions and energy cost

In the calculation of the conversions, a gas expansion factor is used to account for errors made in the GC measurements, as explained in section 1.3 above. The experimental results (CO_2, CH_4 and total conversion and energy cost) with and without the gas expansion factor are displayed in Figures S.8 – S.10. The effect of the expansion factor is most visible at lower O_2 fractions, but overall the effect is rather small in this case. This is attributed to the relatively small fractions of CO_2 and CH_4 used in the experiments. For example, when 100 % of the CO_2 would be converted, there would be only a 5 % gas expansion, as there is originally only 10 % CO_2 present (and 1 CO_2 molecule converts into 1.5 molecules, i.e., 1 CO and ½ O_2). The effect of the gas expansion factor is thus not so important in this case, however, when using high fractions of CO_2 and CH_4, the effect can be very prominent. Many papers in literature do not account for this gas expansion factor, leading to overestimated conversions and too low energy costs.
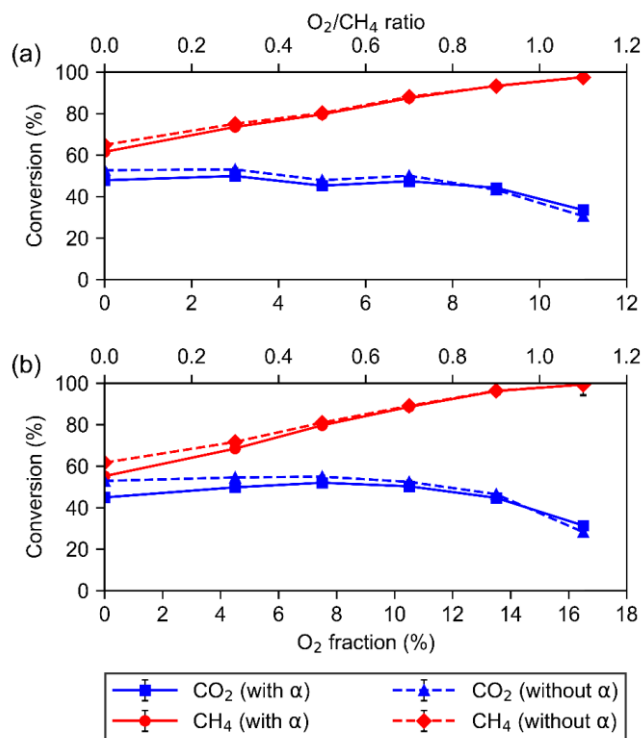
Figure S.8: Experimental CO_2 and CH_4 conversion with and without the gas expansion factor α, as a function of the O_2 fraction and O_2/CH_4 ratio, for a CH_4 fraction of 10 % (a) and 15 % (b). The error bars are too small to be visible.
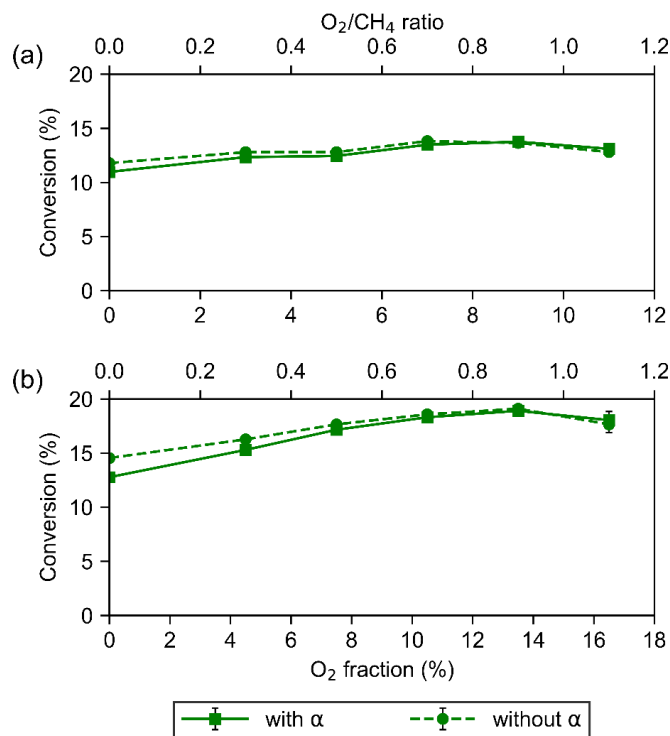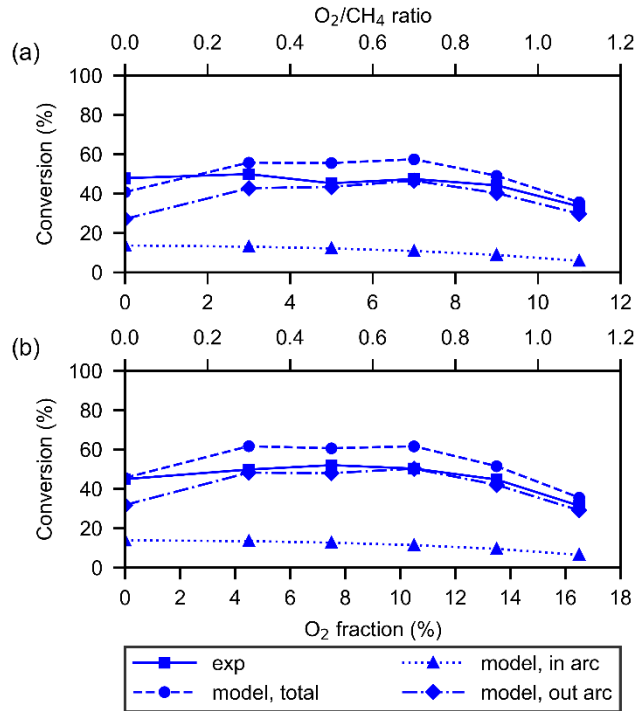

Figure S.9: Experimental total conversion with and without the gas expansion factor α, as a function of the O_2 fraction and O_2/CH_4 ratio, for a CH_4 fraction of 10 % (a) and 15 % (b). The error bars are too small to be visible.
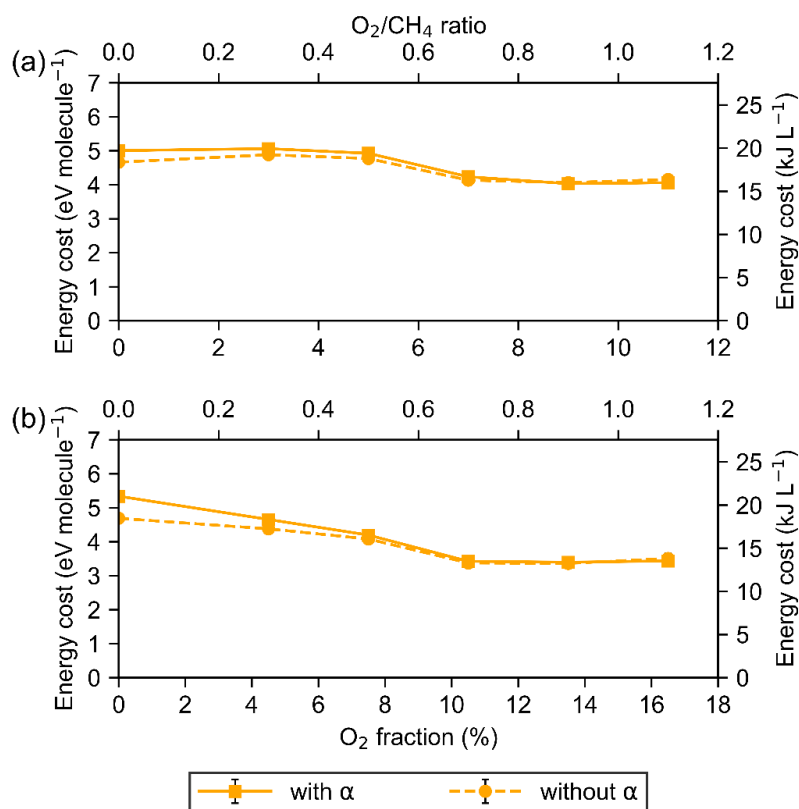
Figure S.10: *Experimental energy cost with and without the gas expansion factor α, as a function of the O_2 fraction and O_2/CH_4 ratio, for a CH_4 fraction of 10 % (a) and 15 % (b). The error bars are too small to be visible.*

3.5 Calculated overall CO_2 and CH_4 conversion in the GAP reactor, inside and outside the arc

Figures S.11 and S.12 present the calculated CO_2 and CH_4 conversions, respectively, in and outside the arc region, as a function of the O_2 fraction, for both 10 and 15 % CH_4, as well as the sum of both and the comparison with the experimental data. Inside the arc, the maximum CO_2 conversion is reached without O_2 present in the mixture, and it decreases with rising O_2 fraction, for both CH_4 fractions. The CO_2 conversion outside the arc shows a broad maximum at an O_2 fraction between 3 – 9 %, with minima at the highest and lowest O_2 fraction. The conversion outside the arc accounts for a larger part of the total conversion, as a result of the much larger fraction of gas that is not passing through the arc.[1,5] The modelling results slightly diverge from the experiments, in terms of profile as a function of the O_2 fraction, which is mostly the result of the conversion outside the arc. This could be attributed to the chosen temperature profile (see section 2.3 above), which could be adjusted to achieve a better fit. However, the aim of this work is not to obtain exact agreement by fitting the data, but to explain the underlying chemistry, which can still be done with these results, as the overall trend is similar.
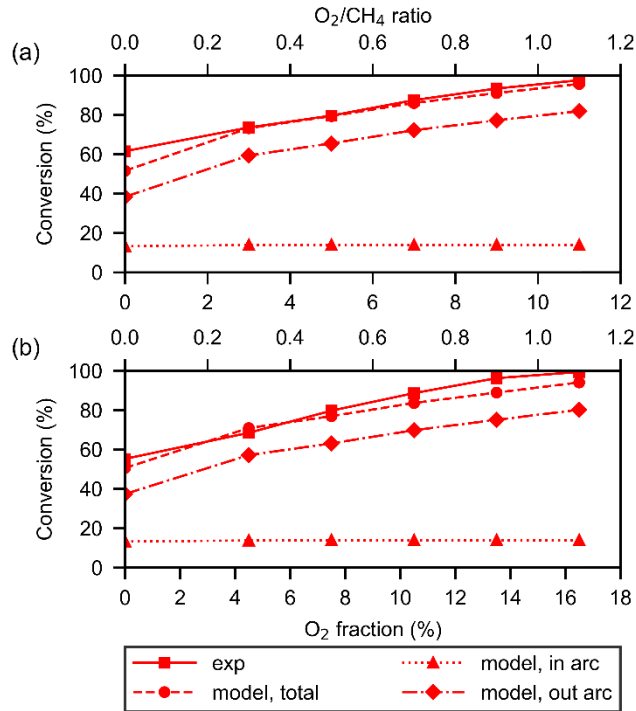
Figure S.11: *Modelling (inside and outside the arc and sum of both) and experimental result for the CO_2 conversion as a function of the O_2 fraction and O_2/CH_4 ratio, for a CH_4 fraction of 10 % (a) and 15 % (b).*

The CH_4 conversion inside and outside the arc is presented in Figure S.12. For all gas mixtures investigated, our calculations reveal that nearly all CH_4 in the arc is converted. However, this results in only 13.8 % of the overall conversion being achieved in the arc. Indeed, the latter is defined by the fraction of gas passing through the arc, obtained from 3D fluid dynamics simulations.[30] Thus, a large fraction of CH_4 is not passing through the arc, but it is still converted, and even much more than for CO_2. Furthermore, Figure S.12 shows that it clearly increases with the O_2 fraction.

This approach to 0D modelling of the GAP reactor, accounting both for the conversion inside and outside the arc, has been used before for a mixture of CO_2 and CH_4.[13] In this former research, mixtures of CO_2 with different CH_4 fractions were tested. For 10 % CH_4 and 90 % CO_2, an absolute conversion of around 14 % was reached for CO_2. This is much lower than the conversions reached in our work, which is attributed to the (nearly) equal fractions of CH_4 and CO_2 (either 10 % and 10 %, or 15 % and 10 %, respectively) in our study, making that more CH_4-derived plasma species are available for contributing to the CO_2 conversion.[32] Furthermore, the addition of N_2 can also help with the CO_2 conversion, as demonstrated in previous modelling work.[23–25] In section 3.9 below, we will elucidate the exact reason for the enhanced CO_2 conversion. Also, for the CH_4 conversion, lower values were obtained in the earlier research, i.e., for 10 % CH_4 and 90 % CO_2, a conversion of around 50 % was reached. This is attributed to the presence of O_2 in our study, which greatly contributes to the CH_4 conversion.

Figure S.12: Modelling (inside and outside the arc and sum of both) and experimental result for the CH_4 conversion as a function of the O_2 fraction and O_2/CH_4 ratio, for a CH_4 fraction of 10 % (a) and 15 % (b).

3.6 Calculated CO_2, CH_4, CO and H_2 density profiles in the GAP reactor, inside and outside the arc
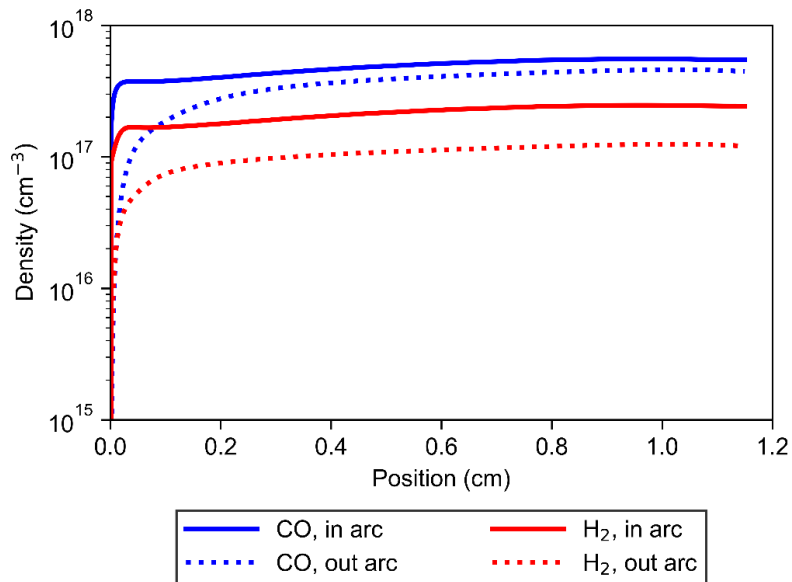
The calculated density profiles of CO_2 and CH_4, as well as of the major products, CO and H_2, as a function of position in the reactor, both inside the arc and in the region around the arc, are plotted in Figures S.13 and S.14, for an intermediate gas mixture of 73 % N_2, 10 % CH_4, 10 % CO_2 and 7 % O_2, Inside the arc, there is a sharp drop of two orders of magnitude in the first micrometres for both CO_2 and CH_4, indicating that these gases are almost immediately converted in the arc. The CO_2 density remains almost constant in the remaining part of the arc, while the CH_4 density first drops further to very low values, after which the density slightly rises again up to the end of the arc. Outside the arc, again most CO_2 and CH_4 react away immediately, although the drop is less drastic than inside the arc, and the densities stay rather constant till the end.
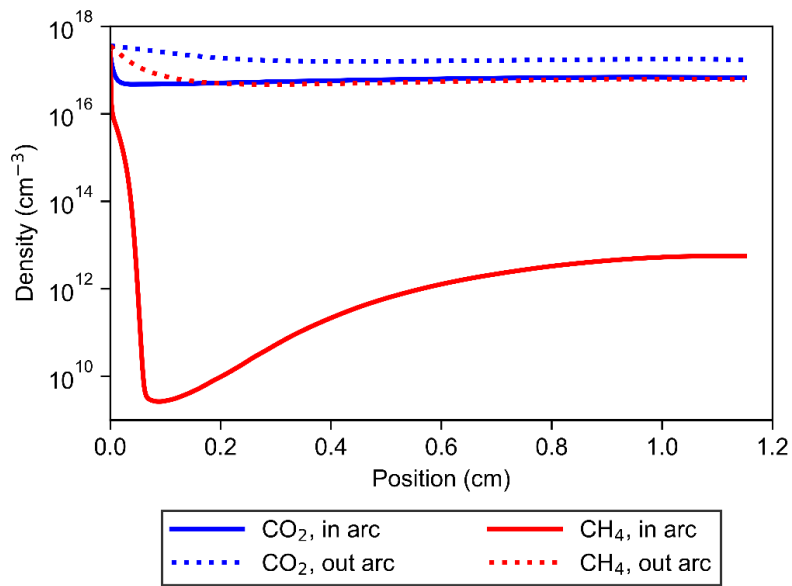
Figure S.13: *Calculated density profiles of CO₂ and CH₄ as a function of position is the reactor, both inside the arc (solid lines) and in the area around the arc (dashed lines). The cathode end is at position 0 cm and the anode edge at 1.15 cm. The densities at the cathode end are 2.5 10^{18} cm^{-3} for both CO_2 and CH_4, both inside and around the arc.*

Similar density profiles were observed for the other gas mixing ratios studied, only with a deeper minimum in the CH_4 density at higher O_2 fractions, because O_2 enhances the CH_4 conversion, as illustrated in the main paper.

The density profiles of CO and H_2 are plotted in Figure S.14, showing an immediate formation in the first micrometres of the arc, and a more gradual rise in the first 2 mm outside the arc. These profiles were similar for the other O_2 fractions in the mixture as well.

Figure S.14: *Calculated density profiles of CO and H₂ as a function of position is the reactor, both inside the arc (solid lines) and in the area around the arc (dashed lines). The cathode is at position 0 cm and the anode at 1.15 cm.*

3.7 Calculated species densities at the end of the GAP reactor, inside and outside the arc, as a function of O_2 fraction

The densities at the end of the reactor for several species, both inside and outside the arc, are plotted as a function of O_2 fraction in Figures S.15 – S.18, at a fixed CO_2 and CH_4 fraction of 10 %. The most important species, i.e., the initial gases CO_2 and CH_4 and the main products CO and H_2, are shown in Figure S.15. The CO_2 density at the end of the arc increases with rising O_2 fraction, while the CH_4 density decreases by five orders of magnitude. This can be explained by the fact that O_2 greatly contributes to the CH_4 conversion, thereby forming again some CO_2. The H_2 density drops by one order of magnitude, while the CO density stays almost constant. The same trends are observed outside the arc, but with a much smaller influence of the O_2 fraction.
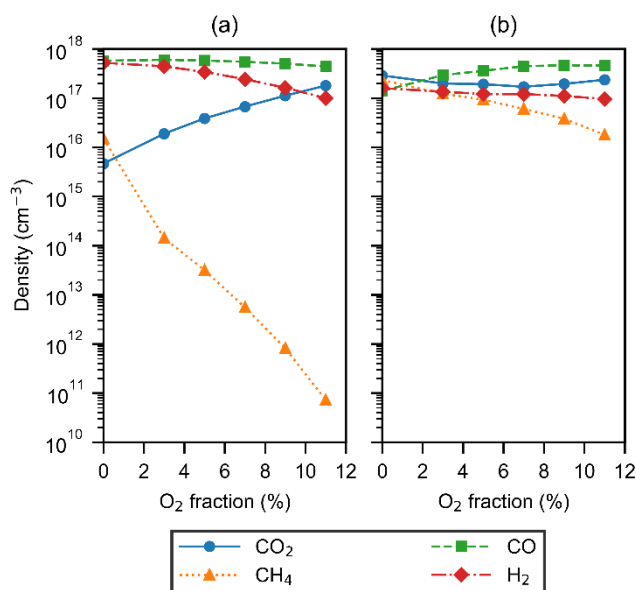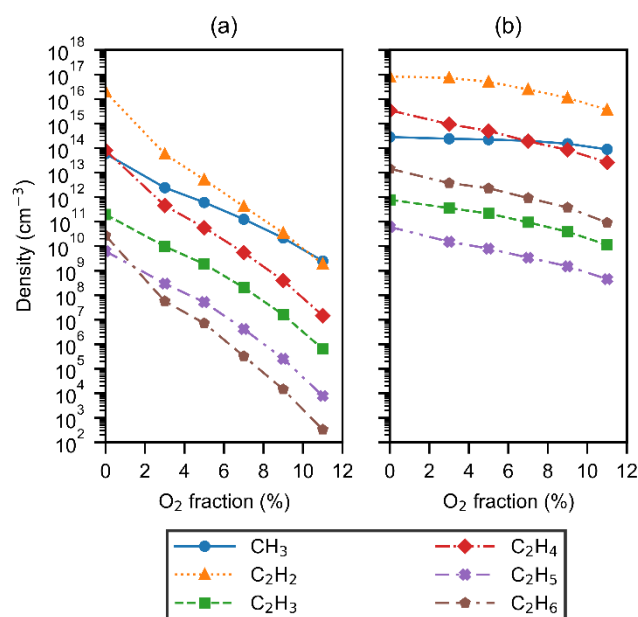

Figure S.15: _Calculated densities of CO_2, CH_4, CO and H_2 as a function of O_2 fraction, at the end of the reactor, inside the arc (a) and outside the arc (b). The y-axes in both graphs are taken the same, to allow easy comparison._

Figure S.16 illustrates the densities of O_2, O, H, OH and H_2O. They all rise with increasing O_2 fraction, which is expected, as they all contain an O atom (and are thus created from O_2), except for H, which is not much affected. Outside the arc, the same trends are observed, but overall the species are formed in lower quantities, which is the result of the lower reactivity (i.e., only thermal conversion and no contribution from the plasma chemistry). The H_2O density is clearly the highest, and even comparable to the CO and H_2 densities (cf. Figure S.15), and it is also very similar both inside and outside the arc. Indeed, it is easily formed from O_2 and the H atoms originating from CH_4 splitting. This will be discussed in more detail below, in section 3.9.
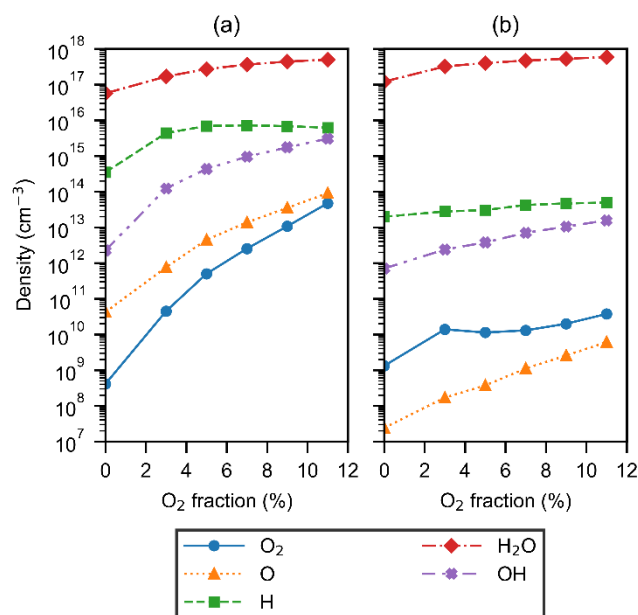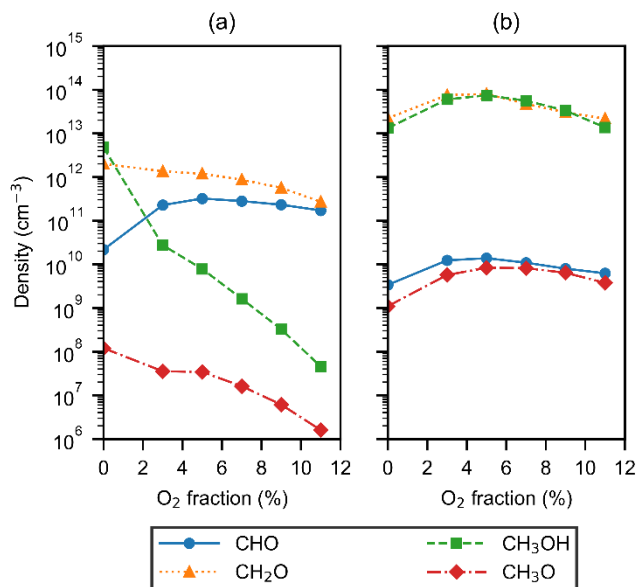
Figure S.16: Calculated densities of O_2, O, H, OH and H_2O as a function of O_2 fraction, at the end of the reactor, inside the arc (a) and outside the arc (b). The y-axes in both graphs are taken the same, to allow easy comparison.

Figure S.17 illustrates the CH_3, C_2H_2, C_2H_3, C_2H_4, C_2H_5 and C_2H_6 densities, which are the result of CH_4 conversion. They reach their maximum when no O_2 is added to the mixture. Indeed, upon O_2 addition, CH_4 is partially converted into oxygenates (including CO and CO_2), and there is less CH_4 left to be converted into hydrocarbons, and thus, the densities of these hydrocarbons decrease upon O_2 addition, both inside and outside the arc. C_2H_2 is formed in the highest concentration, followed by CH_3 and C_2H_4, while C_2H_6 is formed in much lower concentrations. This is in agreement with previous studies for DRM in the GAP[13], and it is beneficial, as C_2H_2 and especially C_2H_4 are more valuable products for the chemical industry than C_2H_6.[33]

Figure S.17: Calculated densities of CH_3, C_2H_2, C_2H_3, C_2H_4, C_2H_5 and C_2H_6 as a function of O_2 fraction, at the end of the reactor, inside the arc (a) and outside the arc (b). The y-axes in both graphs are taken the same, to allow easy comparison.

The higher O_2 fraction in the mixture also generally reduces the formation of oxygenated species included in the model, i.e., CHO, CH_2O, CH_3O and CH_3OH, at least inside the arc, as seen in Figure S.18, although the CHO density goes over a maximum. Outside the arc, all species densities reach a maximum at 5 % O_2. This can be explained because both O_2 and CH_4 are needed to form these oxygenates, but at too high O_2 fractions, CH_4 is further oxidized into CO_2, as demonstrated by the rising CO_2 density in Figure S.15.

Figure S.18: _Calculated densities of CHO, CH_2O, CH_3O and CH_3OH as a function of O_2 fraction, at the end of the reactor, inside the arc (a) and outside the arc (b). The y-axes in both graphs are taken the same, to allow easy comparison._

3.8   Calculated vibrational distribution function (VDF) of CO_2, inside and outside the arc

Figure S.19 illustrates the calculated VDF, based on the 4 symmetric and 21 asymmetric vibrational mode levels, as well as of the ground state of CO_2, at the end of the reactor, both inside the plasma arc and in the area around it, for an intermediate gas mixture of 73 % N_2, 10 % CH_4, 10 % CO_2 and 7 % O_2. Similar results were obtained at the other gas mixing ratios investigated. In addition, we compare these calculated VDFs with the Boltzmann VDF at the gas temperature corresponding to that position in the reactor (i.e., 2113 K inside the arc, and 1828 K outside the arc; cf. Figure S.3).
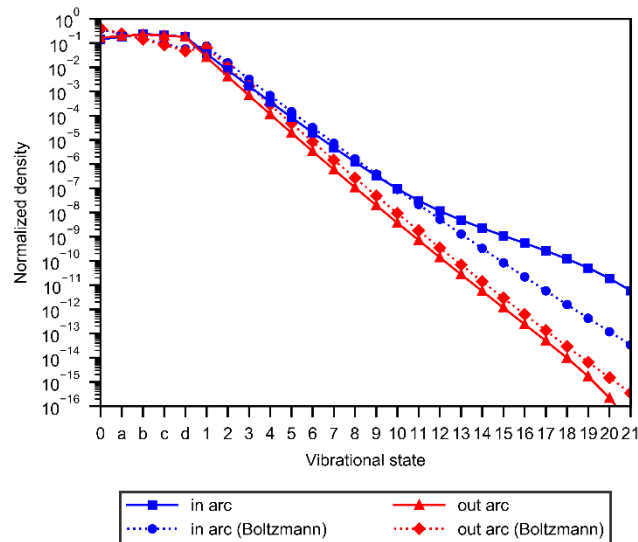
Figure S.19: *Normalized density of the ground state (state 0), 4 symmetric mode and 21 asymmetric mode vibrational levels of CO_2 at the end of the plasma arc (blue solid line) and the area around the arc (red solid line), in comparison with a Boltzmann distribution at the temperature at the end of the plasma arc (blue dashed line) and the area around the arc (red dashed line), showing overpopulation of the higher vibrational levels inside the arc, but a near thermal distribution outside the arc.*

3.9 Reaction pathway analysis of the conversion of CO_2, CH_4 and O_2 into CO and H_2

The contribution for every (production or loss) reaction is calculated as the ratio of the reaction rate for the individual reaction over the sum of all reactions that either produce or consume that species. We will show the results for a CH_4 fraction of 10 % and discuss the influence of the O_2 fraction.

The average reaction rates are used to determine the net rates, which are calculated as the difference between the rates of the forward and reverse reactions. If the reverse reaction has a higher rate, this means that the reaction occurs in the opposite direction and is thus excluded from the analysis of the net (forward) reactions (e.g., loss of CO_2). However, it is then included in the analysis of the reverse reactions (e.g., formation of CO_2). We indeed consider the net rates, because a reaction can have a very high forward rate, but if the reverse reaction has a high rate as well, the net reaction will have little effect on the production or loss of the species involved.

The contribution of the reactions for the production or loss of a species is calculated as the ratio of the net rate of the individual reactions to the total net rate of all production or loss reactions. A cut-off value of 5 % for the relative contribution is applied as a minimum threshold, i.e., reactions for which the contribution reaches this threshold for at least one gas mixture will be taken into account. Some of the reactions occur with a species indicated with "M". These reactions are a combination of various reactions, where M stands for all possible neutral species in the model.

In the figures below, besides the contributions of the individual reactions, a line plot is added, which shows the net (production or loss) rate for that species, so that we do not only have information on the relative contributions of the individual processes, but also on how important they are on an absolute scale. This net (production or loss) rate is calculated as the difference between the sum of the rates of all production reactions and all loss reactions. If there is a net production of the species, this will be added to the figure with the production processes, and vice versa, it will be added to the figure with the loss reactions if there is a net loss of that species. This detailed analysis is performed for the two major inlet gases CO_2 and CH_4 and the two major products H_2 and CO.

The major loss reactions for CO_2, shown in Figure S.20, consist of VV relaxations and vibrational excitations. Note that we thus only consider the CO_2 ground state, although the CO_2 vibrational levels are not really "conversion products", but they typically lead to conversion into dissociation products.

Note also that the sum of the contributions is not yet 100 %, the remaining part is due to many other processes which all have smaller contributions. A small part of the CO_2 is excited in electron impact reactions to V_1 and V_2, but their contribution decreases from 17 % to 6 % with increasing O_2 fraction. The largest part is converted to a symmetric state (V_a) by a reaction with neutral species, with a relative contribution between 33 and 24 %. Other major VV reactions are with vibrational states of CO and N_2, which result in $CO_2(V_1)$. These reactions contribute together for 21 % of the loss of CO_2 without O_2 present, and their contribution increases to more than double (44 %) at an O_2 fraction of 11 %. These major reactions clearly show the start of the ladder climbing process by exciting CO_2 to the first vibrational level. The total net loss rate for the CO_2 ground state is also displayed in Figure S.20, showing a slight decrease with increasing O_2 fraction, in agreement with the behaviour of the CO_2 conversion in the arc, which also decreases with increasing O_2 fraction (see Figure 2 in the main paper).
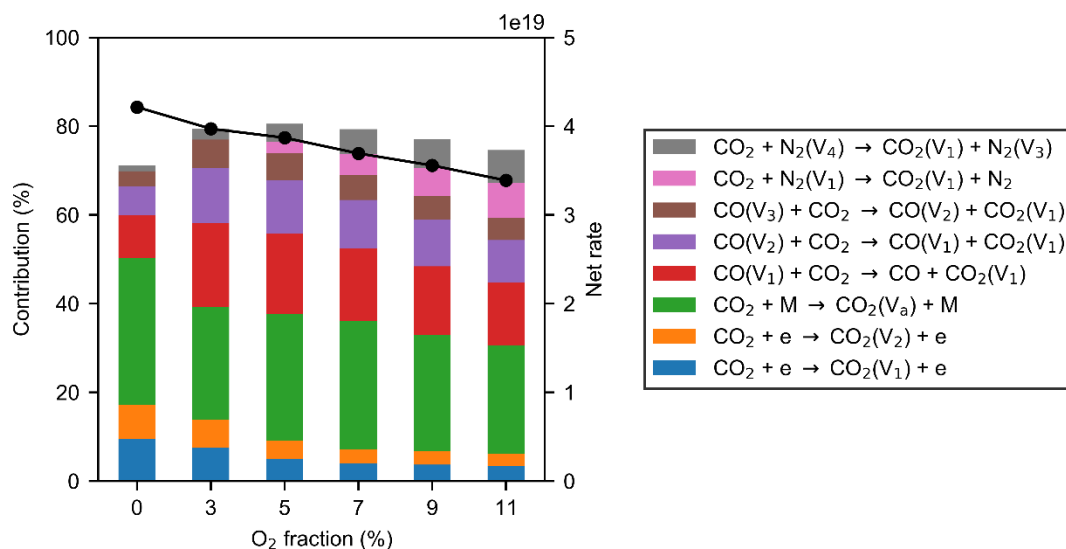
Figure S.20: *Relative contributions of the most important net loss reactions for the CO_2 ground state, at different O_2 fractions and a CH_4 fraction of 10 %. Also shown is the total net loss rate of the CO_2 ground state as a function of O_2 fraction (line plot, right axis).*

Looking at all the reactions that involve CO_2 (production or loss), there is a net loss, but looking at the individual production reactions, some of them cause a net production of CO_2 (Figure S.21). VV and VT relaxations that involve N_2 and vibrational levels of CO_2 play a role when no O_2 is present, but the contributions of these reactions decrease significantly when O_2 is added, from 36 % without O_2 to below 8 % for the mixture with 3 % O_2. There is a very small increase in their contribution at the higher O_2 fractions, but overall their contribution stays below 11 %. The major production reaction for CO_2 [Eq. (22)], certainly when O_2 is present, involves CO and OH where CO can be in the ground or a vibrationally excited state. The relative contribution of this reaction increases when O_2 is added to the gas mixture, from 27 % to 48 %. This is attributed to the much higher density of OH when O_2 is present, see Figure S.16. There is no line plot in this figure, as there is no net production of CO_2.
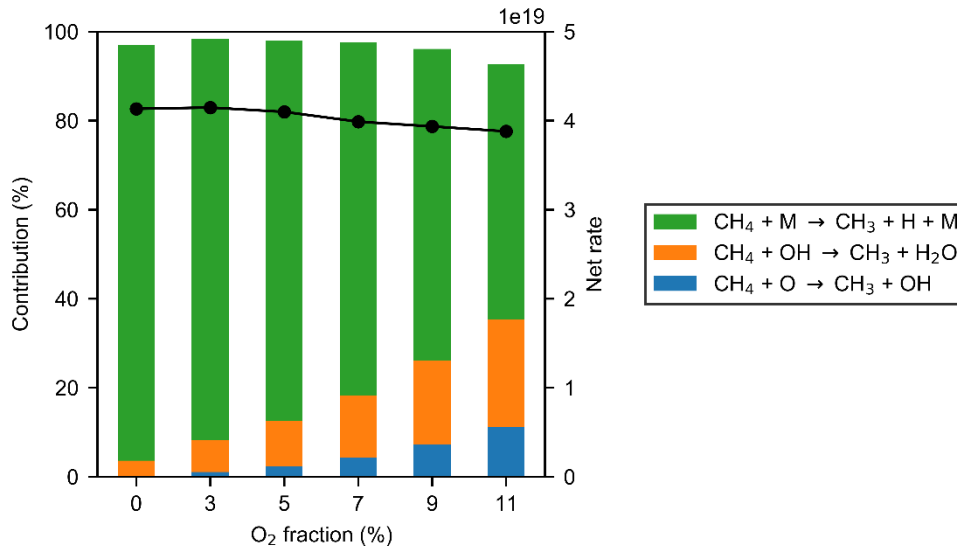
$$CO + OH \rightarrow CO_2 + H \tag{22}$$
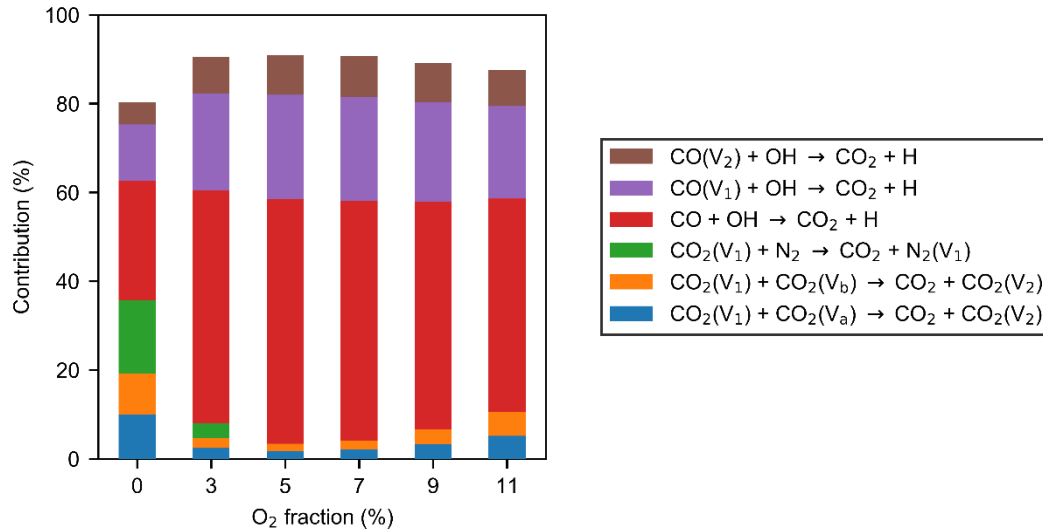
Figure S.21: Relative contributions of the most important net production reactions for CO_2, at different O_2 fractions and a CH_4 fraction of 10 %.

CH_4 is lost mostly through collisions with any neutral molecules M. However, the contribution of these reactions decreases with increasing O_2 fraction (see Figure S.22), while the relative contributions of the reactions with OH [Eq. (23)] and O [Eq. (24)] increase with increasing O_2 fraction.

$$CH_4 + OH \rightarrow CH_3 + H_2O \tag{23}$$

$$CH_4 + O \rightarrow CH_3 + OH \tag{24}$$
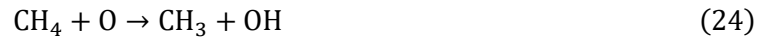
This is logical, as the OH and O densities are higher upon larger O_2 fraction in the mixture (see Figure S.16). The reactions in Equations (23, 24) reach relative contributions of 24 and 11 %, respectively, at 11 % O_2 fraction. Overall, there is a net loss rate for CH_4, but it is little to not influenced by the O_2 fraction, which agrees with the conversion of CH_4 inside the arc (see Figure 2 in the main paper).
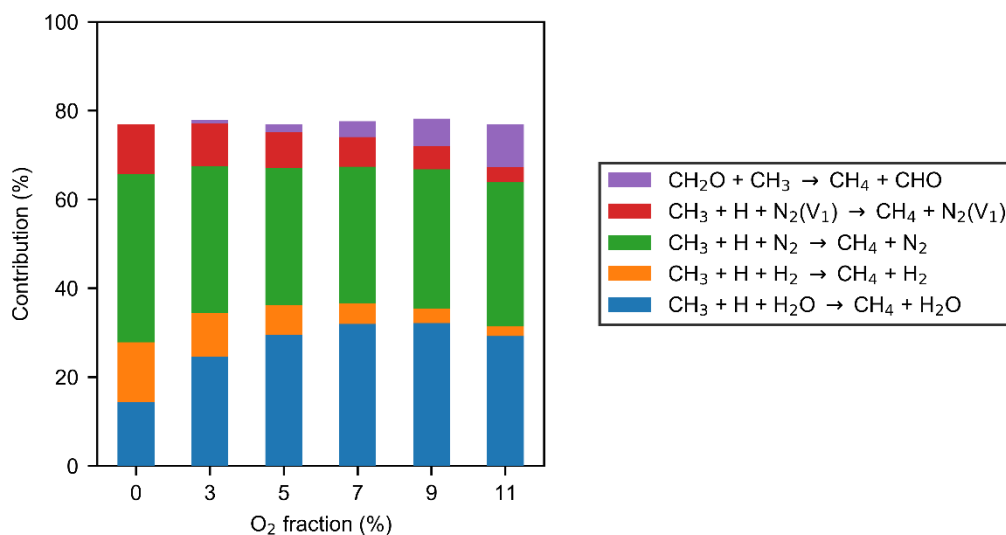

Figure S.22: Relative contributions of the most important net loss reactions for CH_4, at different O_2 fractions and a CH_4 fraction of 10 %. Also shown is the total net loss rate of CH_4 as a function of O_2 fraction (line plot, right axis).

The production of CH_4 is mostly the result of three-body recombination reactions of CH_3 with H, with either H_2, N_2 or H_2O as third body, see Figure S.23. At higher O_2 fraction, the contribution for H_2O rises, as expected, from 14 to 29 %, at 0 and 11 % O_2 fraction, respectively, while the reactions with H_2 and

N_2 decrease with increasing O_2 fraction. Also, other molecules, such as CH_4, CO_2 and O_2, contribute as third body to this recombination reaction, but they are not displayed, because their highest contributions are 4, 3 and 2 % at 11 % O_2 fraction. The reaction with CH_2O [Eq. (25)] is not important without O_2, but becomes increasingly important up to 10 %, at 11 % O_2 fraction.

$$CH_2O + CH_3 \rightarrow CH_4 + CHO \qquad (25)$$

Figure S.23: Relative contributions of the most important net production reactions for CH_4, at different O_2 fractions and a CH_4 fraction of 10 %.

CO is produced by a variety of different reactions, which are based on the relaxation of vibrationally excited CO or the splitting of excited CO_2 (see Figure S.24). The relaxation reactions happen with CO_2, N_2, vibrationally excited states of N_2 or any other neutral species. The contribution of all these reactions decreases with increasing O_2 fraction, while the contribution of the various reactions with CO_2 increases, due to the higher density of CO_2 upon higher O_2 fraction (Figure S.15). The overall net production rate of CO decreases with increasing O_2 fraction, resulting in a lower formation of CO at high O_2 fraction (Figure S.24), in corresponding with Figure S.16.
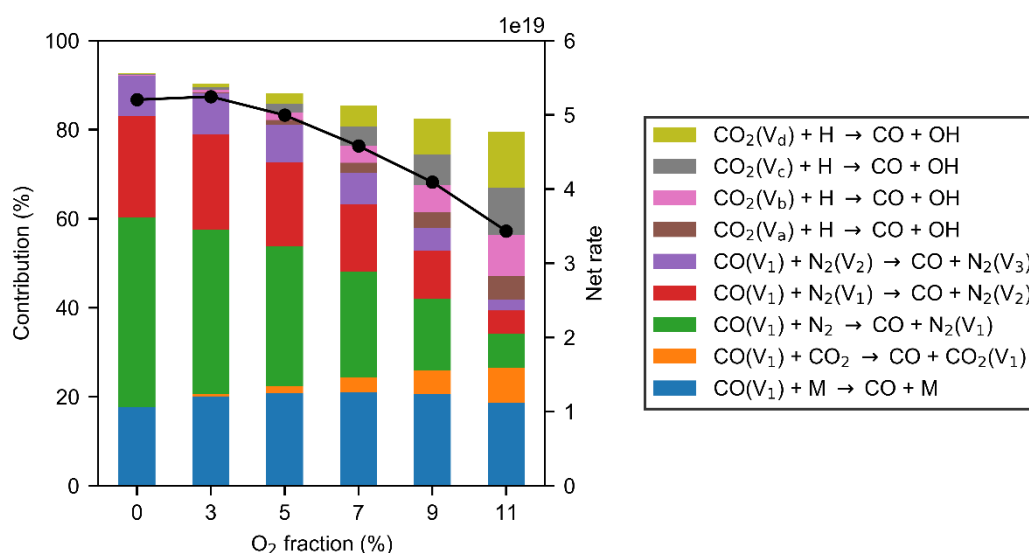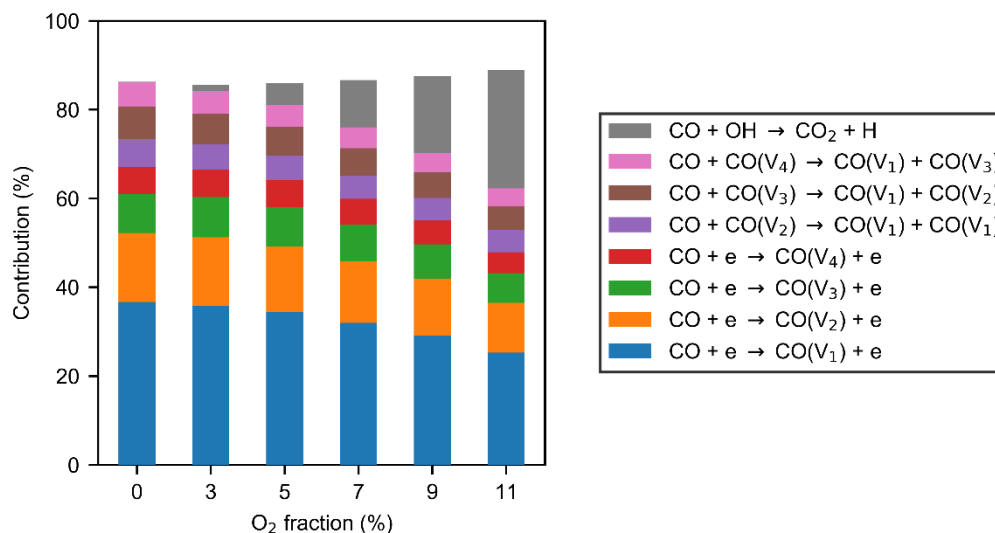

Figure S.24: Relative contributions of the most important net production reactions for CO, at different O_2 fractions and a CH_4 fraction of 10 %. Also shown is the total net production rate of CO as a function of O_2 fraction (line plot, right axis).

The loss processes of CO proceed mainly through vibrational excitation, either by VV reactions with vibrational CO or by electron impact reactions (Figure S.25). Note that we again consider only the CO ground state in this figure. These reactions are not as significant, as no net new products are formed and these excited states can easily return to the ground state, as seen in Figure S.24. Of all these reactions, electron impact excitation to the V_1-state [Eq. (26)], has the highest contribution.

$$CO + e \rightarrow CO(V_1) + e \tag{26}$$

The contribution decreases from 37 % without O_2, to 25 with 11 % O_2 fraction, and this trend is similar for the other loss reactions as well, except for the recombination reaction of CO and OH, which produces CO_2. The contribution of this reaction increases significantly from 0.2 to 27 % at 0 and 11 % O_2 fraction, respectively.
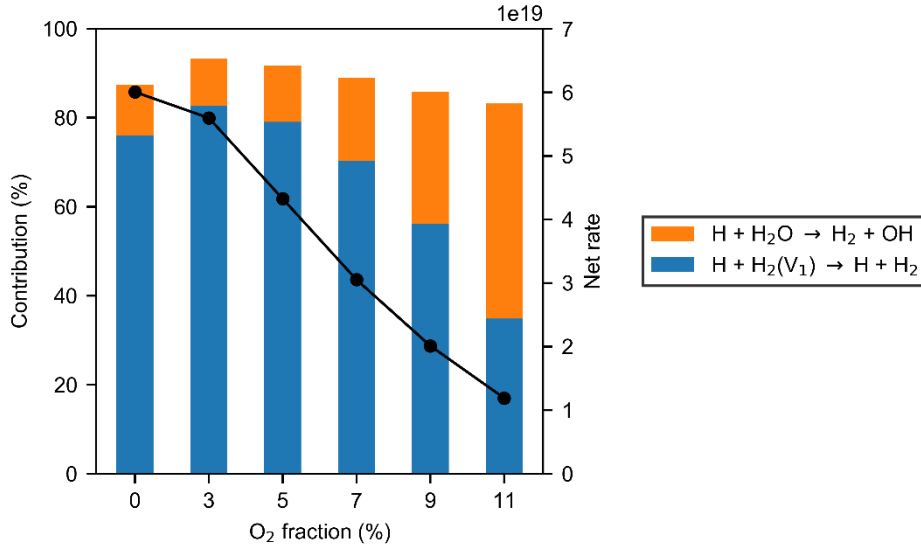

Figure S.25: Relative contributions of the most important net loss reactions for CO, at different O_2 fractions and a CH_4 fraction of 10 %.

The production of H_2 is mainly determined by only two reactions, as seen in Figure S.25.

$$H + H_2(V_1) \rightarrow H + H_2 \tag{27}$$

$$H + H_2O \rightarrow H_2 + OH \tag{28}$$

The vibrational relaxation [Eq. (27)] is not as interesting in the sense that is does not result in the net production of H_2. The reaction in Equation (28), however, is more interesting, and its contribution increases from 11 to 48 %, from 0 to 11 % O_2 fraction, respectively. The rising contribution of this reaction can be related to the increasing H_2O density at a higher O_2 fraction (see Figure S.16). There is a net production of H_2, as seen from the line plot in Figure S.26, but it sharply decreases with increasing O_2 fraction. This corresponds to the decreasing H_2 density upon higher O_2 fraction, see Figure S.15.

Figure S.26: Relative contributions of the most important net production reactions for H_2, at different O_2 fractions and a CH_4 fraction of 10 %. Also shown is the total net production rate of H_2 as a function of O_2 fraction (line plot, right axis).

The loss of H_2 can largely be attributed to electron impact vibrational excitation [Eq. (29)] (see Figure S.27). The contribution of this reaction decreases from 86 to 51 %, from 0 to 11 % O_2 fraction. This reaction, however, does not result in a net change and is just the opposite of the relaxation reaction for H_2 formation (Figure S.26). Besides this reaction, H_2 is lost via some other reactions, among others the reaction with O, forming H and OH [Eq. (30)]. This reaction is only important at high O_2 fractions, the contribution at 7 % O_2 is 4 % and it increases to 24 % at 11 % O_2 fraction. This again can be related to the higher O density upon higher O_2 fraction (see Figure S.16).

$$e + H_2 \rightarrow e + H_2(V_1) \tag{29}$$

$$H_2 + O \rightarrow H + OH \tag{30}$$
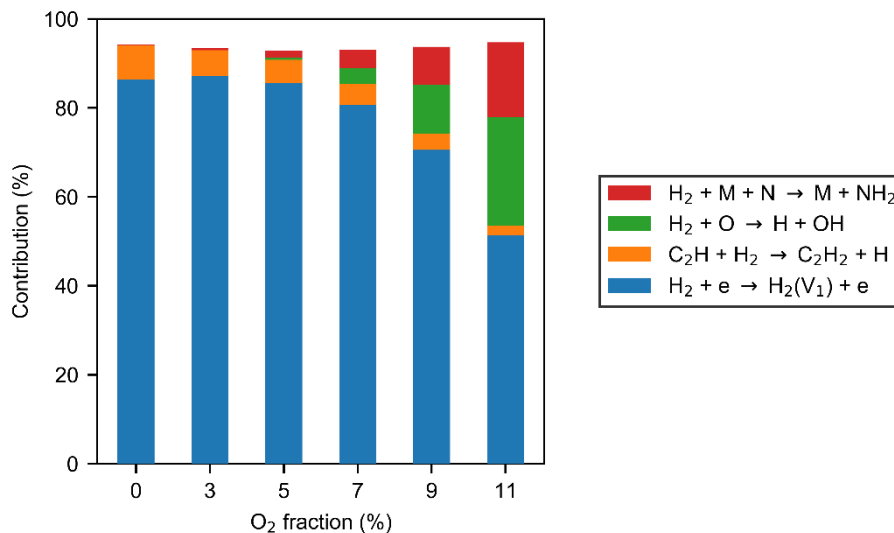
Figure S.27: Relative contributions of the most important net loss reactions for H_2, at different O_2 fractions and a CH_4 fraction of 10 %.

These results provide information on the chemistry inside the arc, showing the influence of different reactions on the CO_2 and CH_4 conversion into CO and H_2, and the relation between different species. The overall net rates show a production of CO and H_2, which decreases however with increasing O_2 fraction. This is similar to what is observed for the densities of these species in Figure S.15. However,

in the area around the arc, the influence of O_2 on the densities is smaller (see Figure S.15). Because this area around the arc is responsible for a significant part of the conversion, the overall effect will be smaller.

4   References

1   G. Trenchev, S. Kolev, W. Wang, M. Ramakers and A. Bogaerts, *J. Phys. Chem. C*, 2017, **121**, 24470–24479.

2   F. Rousseac and A. Rousseac, *Chemical Analysis: Modern Instrumentation Methods and Techniques, 2nd Edition*, 2007.

3   H. F. Coward and G. W. Jones, *Limits of flammability of gases and vapors*, united states government printing office, Washington, 1952.

4   C. F. Covrig and C. Neaga, *UPB Sci. Bull. Ser. D Mech. Eng.*, 2012, **74**, 227–234.

5   E. Cleiren, S. Heijkers, M. Ramakers and A. Bogaerts, *ChemSusChem*, 2017, **10**, 4025–4036.

6   N. Pinhão, A. Moura, J. B. Branco and J. Neves, *Int. J. Hydrogen Energy*, 2016, **41**, 9245–9255.

7   R. Snoeckx, W. Wang, X. Zhang, M. S. Cha and A. Bogaerts, *Sci. Rep.*, 2018, **8**, 15929.

8   S. Pancheshnyi, B. Eismann, G.J.M. Hagelaar, L.C. Pitchford, Computer code ZDPlasKin, http://www.zdplaskin.laplace.univ-tlse.fr (University of Toulouse, LAPLACE, CNRS-UPS-INP, Toulouse, France), 2008.

9   M. Ramakers, S. Heijkers, T. Tytgat, S. Lenaerts and A. Bogaerts, *J. CO2 Util.*, 2019, **33**, 121–130.

10   R. Snoeckx, M. Setareh, R. Aerts, P. Simon, A. Maghari and A. Bogaerts, *Int. J. Hydrogen Energy*, 2013, **38**, 16098–16120.

11   G. J. M. Hagelaar and L. C. Pitchford, *Plasma Sources Sci. Technol.*, 2005, **14**, 722–733.

12   C. De Bie, J. van Dijk and A. Bogaerts, *J. Phys. Chem. C*, 2016, **120**, 25210–25224.

13   S. Heijkers and A. Bogaerts, *J. Phys. Chem. C*, 2017, **121**, 22644–22655.

14   S. Heijkers, R. Snoeckx, T. Kozák, T. Silva, T. Godfroid, N. Britun, R. Snyders and A. Bogaerts, *J. Phys. Chem. C*, 2015, **119**, 12815–12828.

15   M. Ramakers, J. A. Medrano, G. Trenchev, F. Gallucci and A. Bogaerts, *Plasma Sources Sci. Technol.*, 2017, **26**, 125002.

16   S. Gröger, M. Ramakers, M. Hamme, J. A. Medrano, N. Bibinov, F. Gallucci, A. Bogaerts and P. Awakowicz, *J. Phys. D. Appl. Phys.*, 2019, **52**, 065201.